Characterization of functional MXene nanocellulose thin films

Ekaterina Shoshinskaia, Lomonosov Moscow State University, Russia

September 4th, 2019

Supervisor: Calvin J. Brett

Abstract

Functional thin films gained wide-spread attention over the last decade due to their unprecedented applicability. Thin film technology can be found in our today's smart generation as e.g. in mobile phones, fitness trackers and modern sensors. Nevertheless, nowadays environmental issues dominate our thoughts. Hence, biodegradable and bio-based products should replace fossil-based materials for a better bio economy. Nanocellulose (CNF) as produced from wood is a great candidate in replacing fossil-based polymeric materials due to is unique properties as e.g. light weight, stiffness, anisotropy. Combining this with novel inorganic two-dimensional carbide material MXene one might build the future electronics with low CO_2 footprint. In this project we performed spray deposition experiments to yield homogeneous nanoscale thin films. The films were characterized using atomic force microscopy (AFM), UV-Vis spectroscopy, and surface sensitive X-ray scattering as GISAXS and GIWAXS. This study shows first correlation how nanoscale one-dimensional building-blocks as CNF and the two-dimensional MXene forms functional thin films. This study shows a facile route which should pave the way for future applications combining bio-based and unique nanoscale materials.

Contents

1. Introduction

In the quest of creating mutli-functional electronic devices such as touch screens, liquid-crystal displays, dye-sensitized solar cells, electrochromic devices, sensors and others, transparent durable conductive electrodes are needed. Due to the excellent optoelectronic properties of indium tin oxide, it is considered the most preferred transparent conductive electrode [1]. But for applications with flexible touch screen and organic light emitting diode, the materials must be mechanically robust. So constant efforts are being made to replace indium tin oxide with alternative materials, such as conductive polymers, metal and carbon-based nanostructures. In addition to excellent optoelectronic and mechanical properties, low cost of production per unit area and feasibility of large-scale fabrication are key factors in determining their industrial success [2-3]. 2D graphene is the most studied material for transparent electrodes application, but for successful commercialization, it has a high fabrication cost and size limitations [4-5]. Recently, a new class of 2D transition metal carbides and/or nitrides, so-called MXenes, was discovered [6]. Most MXenes exhibit metallic conductivity, hydrophilicity, high mechanical strength, and can act as intercalation hosts, as indicate by theoretical and experimental results. The Ti3C2 MXene flakes (Ti3C2Tx, where T stands for O, OH, F, and other surface terminations and x is a number of the terminating groups) possess surface functional groups similar to graphene oxides but offer a much higher electrical conductivity. They have shown great promise as electrodes in supercapacitors, Li-ion and other types of batteries, fuel cells, reinforcement for polymers, adsorbents, and sensors [7]. Upon delamination, colloidal MXene solutions contain large quantities of ≈ 1 nm-thick 2D flakes with lateral sizes up to several micrometres, which are perfect for solution processing [8].

Further, over the last decades sustainable materials have gained increasing attention for future flexible, biodegradable, yet disposable electronics [9-12]. Cellulose nanofibers (CNF) has favourable properties such as lightweight, thermal stability, and good mechanical strength. These properties make CNF a very promising precursor for creating of high-performance bioinspired materials and nanocomposites due to their earth abundant bio-based origin and biocompatibility. The disadvantages of bio-based materials, compared with some fossil-based materials are still systematic quality control, influence of solvent absorption and a limited lifetime. But CNFs are already finding their way to a wide range of applications from transparent conductive nanopaper to ultra-strong bio-active fibers [13-16]. In such applications surface roughness and porosity is an important factor that affects the device compatibility, as high surface roughness may lead to inhomogeneities and a decrease in performance for thin film-based applications as optoelectronic devices.

2. Theory

2.1.Materials

2.1.1. Cellulose

In recent years, the synthesis and application of nanocellulose draw a lot of attention for use in high-performance biomaterials. Cellulose is referred as nanocellulose, when one dimension is around 3-5 nm and has a length of a few hundred nanometres up to a few micrometer [17]. Cellulose nanofibrils (CNF) are high-aspect ratio nanoparticles with molecular high stiffness and mechanical performance, which makes them excellent materials to build macroscopic materials from them [18]. It is considered a sustainable material due to its biodegradable nature. Depending on the technique and synthesis conditions of nanocellulose, which determines its dimensions, composition and properties, it can be divided into three main categories: cellulose nanocrystals (CNCs), and CNFs. Earlier CNF producing was considered an expensive process due to the high energy demands required in mechanical disintegration. However, with the discovery of 2,2,6,6-tetramethylpiperidine-N-oxyl (TEMPO)-mediated oxidation [19], which have eased the mechanical disintegration process, CNF has become a more attractive material for commercial applications. Nowadays there are several companies around the globe producing TEMPO-CNF in few hundred kilogram scale per day.

2,2,6,6-Tetramethylpiperidine-1-oxyl radical TEMPO-CNFs are long entangled fibrils with a diameter in nanometer range. Typically, they have a diameter of 5–50 nm and a length of a few micrometers [20]. These cellulose nanofibers always contain uniform width (3–4 nm) with a high aspect ratio which can be applied as transparent and flexible display, gas-barrier film for packaging, and nanofiber filling for composite materials [21] TEMPO-CNFs are produced by chemical treatments of cellulosic pulp suspension.

In this work we used TEMPO-CNF after Isogai et al. [21] procedure with specific surface charge of 1360 μmol/g. We yield a water CNF suspension with 0.3 wt% solid content after microfluidizer. The CNF suspension is further diluted with water (1:20), mixed in a UltraTURRAX at 10.000 rpm for 15 min, followed by ultra-sonication for 15min and 60min of centrifuging at 3000 rpm. The final suspension was then used for the spray deposition experiments.

2.1.2. MXene

MXenes are a rapidly growing family of 2D transition metal carbides, nitrides, and carbonitrides with the general formula $M_{n+1}X_nT_x$ (n = 1, 2, or 3; M = transition metal, e.g., Ti, V, Nb, Mo; X = C and/or N; T = surface termination, e.g., –OH, –F, =O) [22]. It has high flexibility, ease of dispersing in water and high volumetric capacitance. For both device applications and fundamental studies, MXene samples are generally thin films comprised of many MXene flakes, though some studies have focused on single-layer MXene. In contrast to most other 2D materials, MXenes offer an attractive combination of high electronic conductivity, hydrophilicity, and chemical stability [23]. With these properties, MXenes show exceptional promise in areas including electromagnetic interference shielding, wireless

communication, chemical sensing, energy storage, optoelectronics, triboelectrics, catalysis, and conformal/wearable electronics.

The MXene suspension was synthesized using the preparation protocol early described in [24] with hydrofluoric acid as an etching agent and tetramethyl ammonium hydroxide (TMAOH) solution for delamination. Ti_3AlC_2 phase purchased from Advanced Ceramic Esoterica (China) was used as a starting material, other reagents were purchased from Sigma-Aldrich and were used without further purification.

2.1.3. Silicon wafer

Silicon wafers were used as a substrate for spraying. Previously, Piranha cleaning was provided according to a standard procedure [25] followed by keeping the wafers in distilled water. Before use, the silicon wafers were washed with distilled water and dried using N_2.

2.2.Spray deposition

Spray coating is the technique to deposit films on substrates out of solution by using a pressure controlling system. The crucial parameter of the structure of the liquid in the nozzle is the flow rate of the aerating gas, closely related to the pressure applied in spraying [26]. Increasing this flow rate, decreases the liquid content in the nozzle surrounding the gas flow, and decreases the droplets' size. This homogenizes the spray deposition, but significantly only up to an optimum gas-to-liquid mass flow ratio. With increasing viscosity of the suspension, the liquid phase is enriched at the walls of the nozzle, and an annular flow is formed. The two-phase flow passes a nozzle, which leads to rapid expansion. Due to the expansion after the nozzle, a cone develops, thus the droplet density decreases from the dense region to the dilute and very dilute region [27]. Via the gas stream, the droplets are transported to the samples surface. During the transport period solvent evaporation from the droplets occurs, leading to shrinkage of the droplets. Finally, the pressure of the gas and the viscosity of the solution have to be considered. The pressure of the gas plays an important role during spray coating, as it influences the transport of the droplets to the surface and thus the film formation conditions. Higher gas pressure will lead to an increased interaction of the gas flow with the surface. Via the gas stream, the droplets are transported to the samples surface. During the transport period solvent evaporation from the droplets occurs, leading to shrinkage of the droplets. Hence, nozzle-to-sample-distance NSD must be increased. Flow rates can also be increased via volatile solvents, but lead to larger droplet sizes. Mandal et at. [28] showed the influence of shear behaviour of the fluid on the spray deposition parameters, especially cone geometry was considered. For shear-thinning in Newtonian to shear-thickening fluids, the spray cone angle decreases. After deposition of the liquid, the solvent evaporates and leaves behind a nanostructured surface. The droplet impact on a hot surface was previously investigated by Kompinski et al. [29]. This is especially important for the deposition at elevated substrate temperatures. The deposited layer thickness is strongly dependent on flow rate, spray time and concentration of material. Next, the principle of the spray installation will be described.

Gas at a pressure of 6 bar is supplied from a gas bottle. Since the distance between the gas source and the spray device is large, a delay is formed, which leads to improper processes. To eliminate this defect, an additional reservoir was installed. Next, a device for controlling gas

supply (magnetic valve) is installed. Then, the gas flows through two tubes: one to open a shutter in the spray-device, and the other one to drag the solution out of sample reservoir. Figure 1.

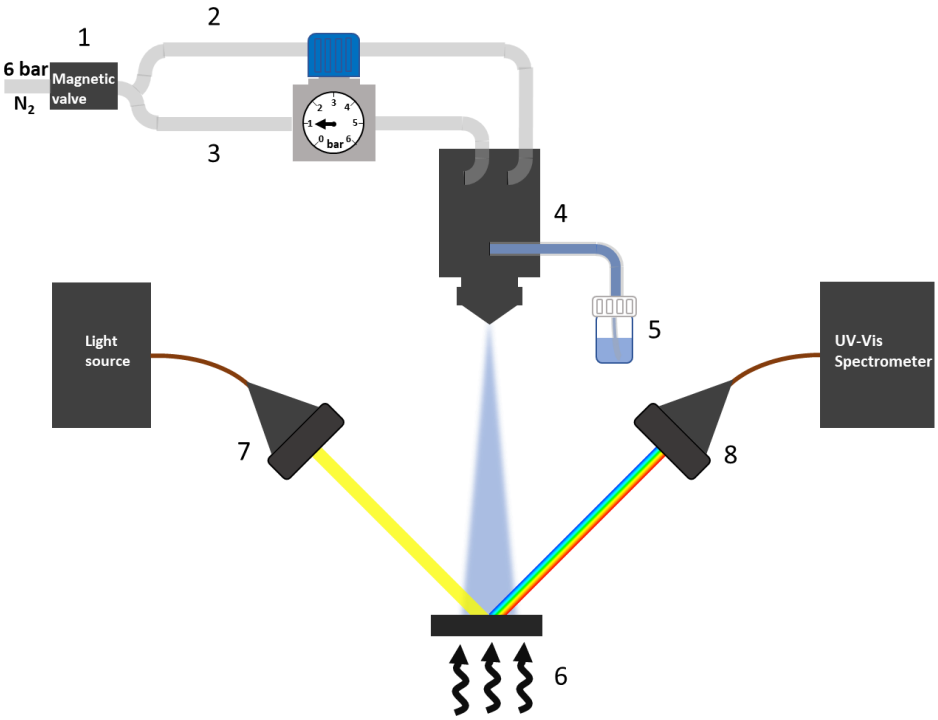

Figure 1. Spray setup and UV-VIS spectroscopy. 1 – magnetic valve; 2, 3 – cylinder and sample tubes; 4 – spray device, 5 – sample reservoir; 6 – substrate heater; 7, 8 – UV-vis source and detector. Image copyright Calvin Brett (DESY Hamburg, KTH Stockholm).

The spray deposition was achieved through atomization of the CNF/MXene suspension with compressed nitrogen at a gas pressure of 1 bar. The nozzle-to-substrate distance of 200 mm led to spraying in the very dilute regime [30]. We used a spray protocol as following, 0.01 s spraying, 6 s waiting, in 18 cycles for CNF and 1 cycles for MXene. The Si substrate temperature was controlled to 130 °C.

2.3.AFM

The atomic force microscope (AFM) measurements were performed using a MultiMode MMAFM-2 (Bruker Corporation, USA). The thin films were mapped on (1 × 1) μm^2 areas to check the homogeneity and evaluate the roughness change incorporating the MXene. The AFM was used in tapping mode and the device was equipped with a nitride-based cantilever (Scanasyst-AIR-HR, resonance frequency: 130 kHz, spring constant: 0.4 N/m, tip radius nominal: 2 nm, Bruker Corporation, USA)

2.4.UV-Vis

The UV-vis spectroscopy was recorded using Glacier X (B&Wtek, USA) spectroscope, which is shown in the schematic setup of UV-vis spectroscopy in Figure 1. Measurements were provided for clean silicon wafer (after Piranha cleaning and further cleaning and drying

procedures), CNF sprayed on Si wafer, MXene sprayed on Si wafer and MXene prayed on top of CNF, which was sprayed on Si wafer.

2.5.GISAXS / GIWAXS

GISAXS (grazing incidence small-angle x-ray scattering) and GIWAXS (grazing incidence wide-angle x-ray scattering) are methods were an x-ray beam illuminate a sample surface at a very shallow angle ($\alpha_i < 1^{\circ}$) with respect to the sample plane. The scattering is measured by two-dimensional detectors. On the detector the intensity dependence of the exit angle (or in-plane angle) α_f and the out-of-plane angle Ψ is observed. Plane is the sample plane (xy plane). The x axis is in the plane of the sample and is directed along the direction of projection of the incident X-ray beam onto the plane of the sample, the z axis oriented along the surface normal, the y axis is in the plane of the sample surface as well (Figure 2). The wave vector transfer **q** is given by

$$\mathbf{q} = \boldsymbol{k_f} - \boldsymbol{k_i} = \frac{2\pi}{\lambda}\begin{pmatrix}\cos(\alpha_f)\,cos(\Psi) - \cos(\alpha_i)\\ \cos(\alpha_f)\sin(\Psi)\\ \sin(\alpha_i) + \sin(\alpha_f)\end{pmatrix},$$

where λ is the wavelength, $k_i = 2\pi/\lambda$ and k_f are incident wavevector and scattered wavevector correspondingly.

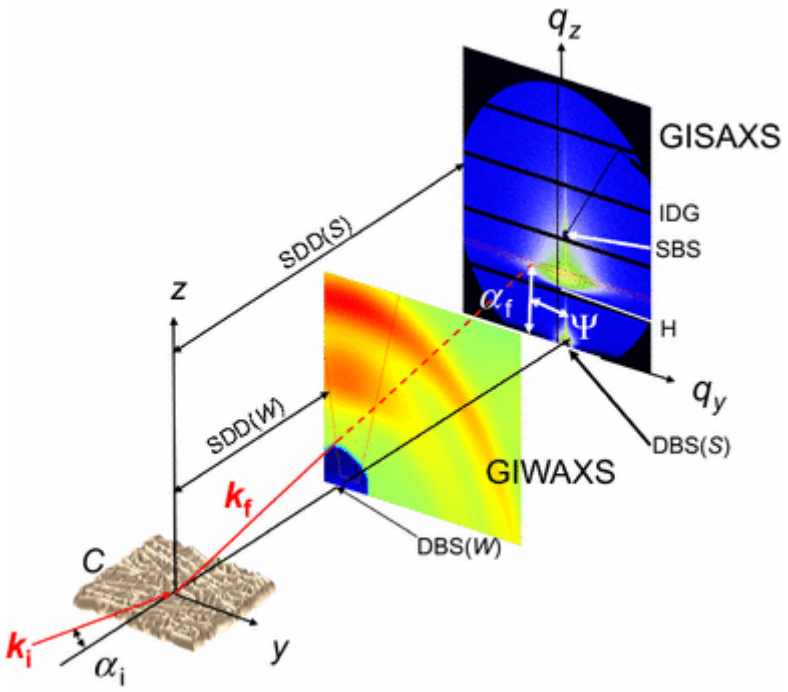

Figure 2. Schematic setup of the grazing incidence small- and wide-angle X-ray scattering (GISAXS/GIWAXS). y, z denotes a real-space coordinate system. q_y, q_z denotes a reciprocal space coordinate system. C denotes the sample. SDD(W, S) are sample-detector distance for the GIWAXS and GISAXS case. IDG denotes the intermodular gap of the two-dimensional Pilatus detector. DBS(W, S) and SBS denote the beamstop for the direct beam for GIWAXS

and GISAXS and the specular beamstop in GISAXS geometry. H denotes the sample horizon. [31]

GISAXS/GIWAXS measurements were provided at the PETRA III synchrotron at DESY (Hamburg, Germany), beamline P03. For The SDD(S) = (2674 ± 1) mm, the SDD(W) = (129 ± 1) mm with an incident photon wavelength of λ = 0.986 Å (hv = 12.575 keV), beam size of H × V, (15 × 21) μm^2 and the X-ray angle of incidence was set to $\alpha_i = (0.40 \pm 0.01)^{\circ}$. 1D intensity distributions were extracted from the 2D GISAXS/GIWAXS pattern using the DPDAK software package.

3. Measurement / Discussion

3.1. AFM

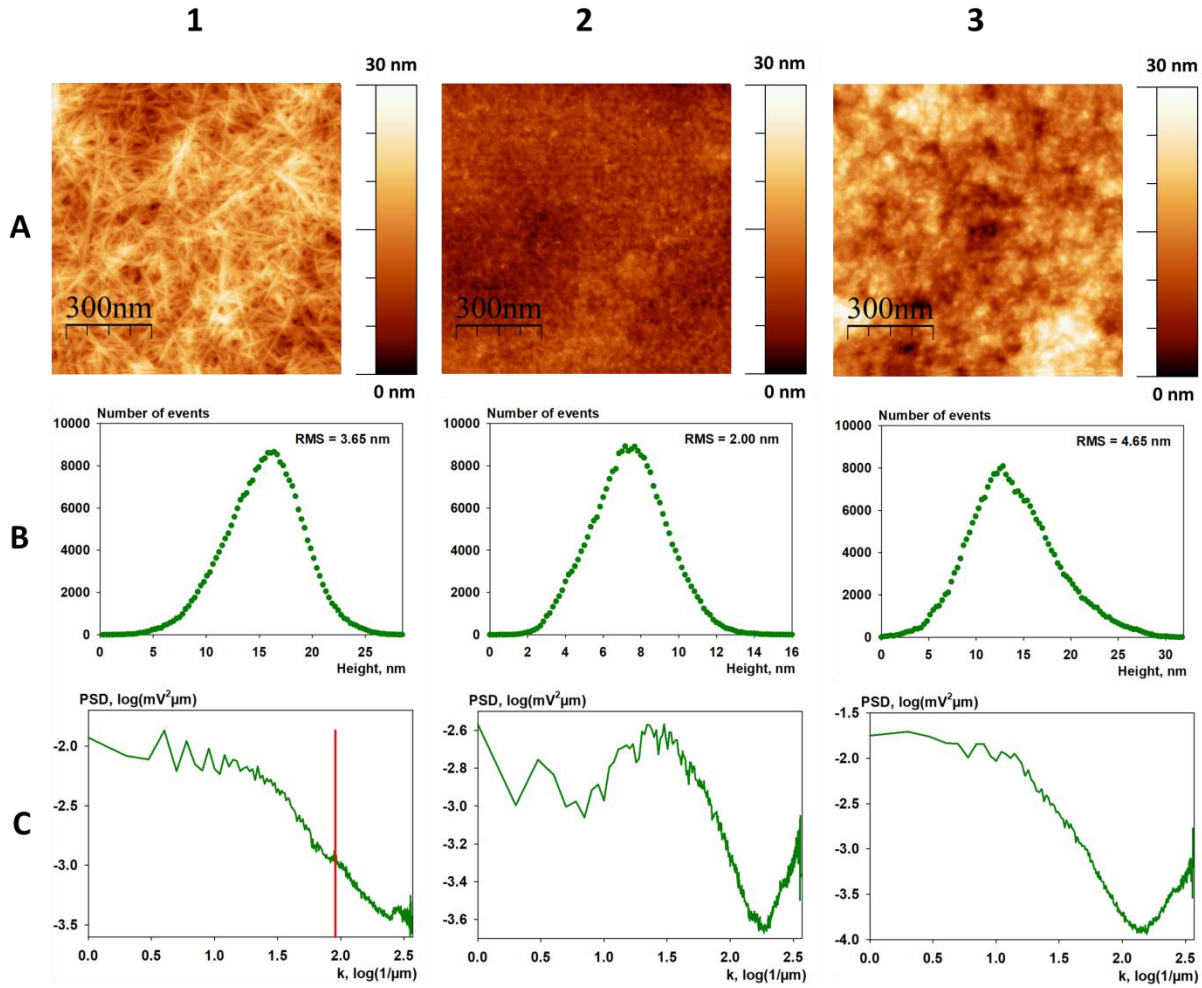

Figure 3. AFM data: CNF 1x1 μm^2 1360 height diagram (1A), FFT diagram (1B), roughness analysis (1C); MXene 1x1 μm^2 height diagram (2A), FFT diagram (2B), roughness analysis (2C); MXene on CNF 1x1 μm^2 height diagram (3A), FFT diagram (3B), roughness analysis (3C).

AFM measurements were performed for CNF, MXene and MXene on top of in the region of 1 x 1 μm^2. The results of measurements and data processing are presented in Figure 1. As one can see (1A), the cellulose looks like long thin fibers, whereas in the sample where MXene are

on top of the cellulose, the fibers are not observed. We speculate that there is lot of Mxene on top of the cellulose or the CNF is fully surrounded by MXene. Probably, Mxene solution should be more diluted to observe CNF beneath it. One can also observe that the peak-to-valley height of the sample of Mxene on top of cellulose increased compared to the other two samples (only CNF and only MXene), looking at the roughness analysis (Fig. 3, line B). The maximum height value of CNF sample is 28.5 nm, of MXene sample is 16.5 nm and of Mxene-on-CNF sample is 31.7 nm. If one looks at PSD plot of CNF (Fig. 3, 1C), a step in the area of the red vertical line is observed. It can be interpreted as the presence of some standard distance between sample domains (11.03 nm corresponds to the distance). As an additional confirmation, the profile from CNF (Fig. 4) was plotted. As one can see, the distance between fibers is 9.76 nm.

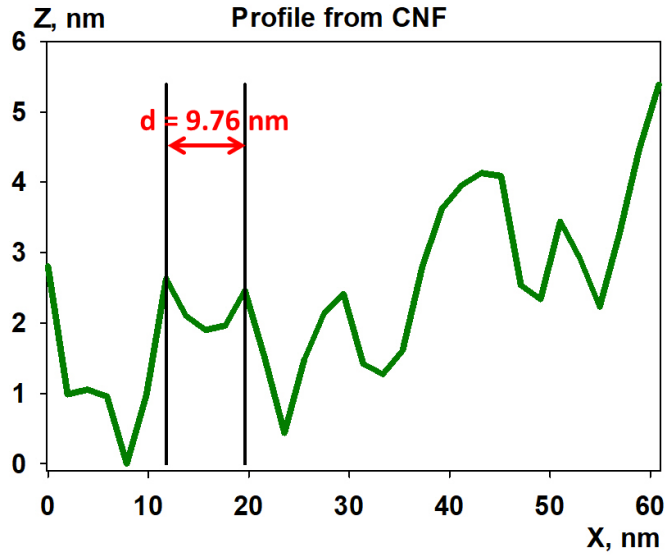

Figure 4. Profile from CNF height diagram. X is the profile direction, Z – height.

3.2.UV-Vis

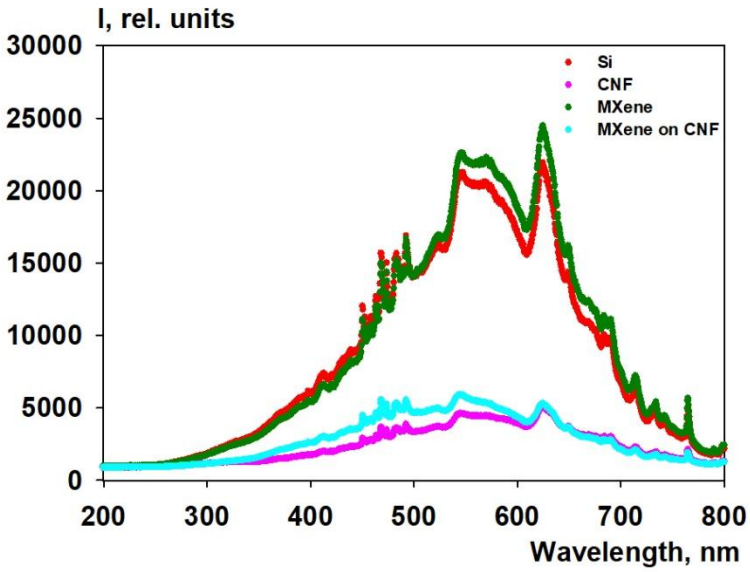

Figure 5. UV-VIS spectrometry data of silicon (red), CNF (magenta), MXene (green) and MXene on CNF (blue) in the range of 200-800 nm.

The setup for the UV-VIS spectrometry experiment is shown in Figure 1. For each sample, reflection spectra were taken (Figure 5). According to the spectra, the reflectivity of CNF and MXene on top of CNF is lower than that of the silicon wafer, while the reflectivity of sample on which only MXene was sprayed is larger than that of silicon.

3.3.GISAXS/GIWAXS

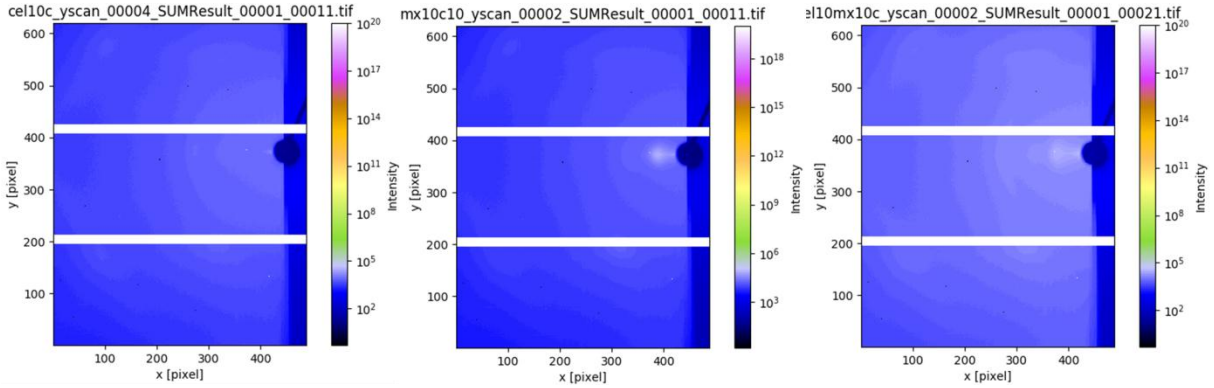

Figure 6. GIWAXS images for CNF, MXene and MXene on CNF.

GIWAXS images are presented on Figure 6. As one can see, in the region of 400 pixels of the x-axis there are differences. These differences occur due to the packing of the 2D MXene on top of each other. The peak position than directly relates to the distance of these MXene sheets to each other. This phenomenon should be further elucidated in a continuation of this project.

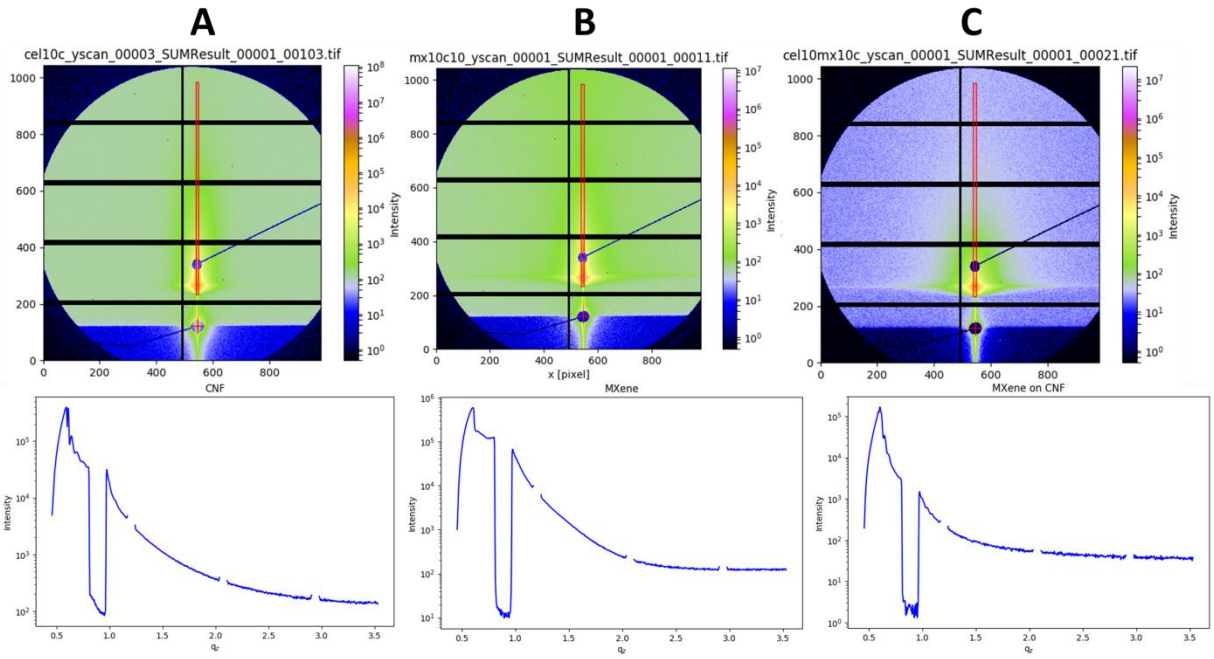

Figure 7. GISAXS data and under it the vertical cuts which are marked in red boxes within the GISAXS pattern. A – CNF, B – Mxene, C – Mxene on CNF.

Then, GISAXS experiments were provided, the results of which are shown on Figure 7. According to the GISAXS images, a vertical cut was selected using the DPDAK software

package. The curves of the dependence of intensity of q_z for the selected region were plotted. From these curves, one can determine the shape of the particles on the substrate. One can see that there is a difference between MXene on CNF and only CNF structure and also MXene on CNF and only MXene structure. Interestingly, the CNF and MXene on CNF show distinct occilations which stems from correlated layering of the particles to each other. This only occurs when the thin films is very homogeneously spread on a surface and is a confirmation for a nice layering using spray deposition. Further explanations can only be given with proper use of a model fitting the form- and structure-factor within the thin film may using software packages like BornAgain or IsGISAXS.

4. Conclusion

As a result of the work, an advanced remotely controllable spray setup incorporating *in situ* UV-Vis spectroscopy was constructed. Initial samples were prepared using the setup. Subsequential, atomic force microscopy, UV-vis spectroscopy and GISAXS / GIWAXS were mastered and applied to the sprayed samples. Preliminary processing of the obtained data is performed, it was received that the concentration of MXene is too high in order to see individual nanocellulose beneath it. The reflectance spectra of MXene is high, but for the nanocomposite sample using MXene on top of cellulose it is much lower, but still higher than that of cellulose. Nanoscale fibres with high-aspect ratio are observed on the sample with cellulose. On the surface a mean fiber-to-fiber distance of ~10 nm was observed.

One possible continuation on this project should be to use different concentrations of MXene on top to CNF to study the layer and conformation surrounding the CNF.

References

1. T. Gao, Z. Li, P. S. Huang, G. J. Shenoy, D. Parobek, S. Tan, J.-K. Lee, H. Liu, P. W. Leu, ACS Nano 2015, 9, 5440.
2. I. Khrapach, F. Withers, T. H. Bointon, D. K. Polyushkin, W. L. Barnes, S. Russo, M. F. Craciun, Adv. Mater. 2012, 24, 2844.
3. J. Saghaei, A. Fallahzadeh, T. Saghaei, Org. Electron. 2015, 24, 188.
4. Z. Yang, J. Ren, Z. Zhang, X. Chen, G. Guan, L. Qiu, Y. Zhang, H. Peng, Chem. Rev. 2015, 115, 5159.
5. J. D. Roy-Mayhew, I. A. Aksay, Chem. Rev. 2014, 114, 6323.
6. M. Naguib, M. Kurtoglu, V. Presser, J. Lu, J. Niu, M. Heon, L. Hultman, Y. Gogotsi, M. W. Barsoum, Adv. Mater. A. 2011, 23, 4248.
7. M. R. Lukatskaya, O. Mashtalir, C. E. Ren, Y. Dall'Agnese, P. Rozier, P. L. Taberna, M. Naguib, P. Simon, M. W. Barsoum, Y. Gogotsi, Science 2013, 341, 1502
8. M. Naguib, O. Mashtalir, J. Carle, V. Presser, J. Lu, L. Hultman, Y. Gogotsi, M. W. Barsoum, ACS Nano 2012, 6, 1322.
9. Y. H. Jung, T. H. Chang, H. Zhang, C. Yao, Q. Zheng, H. Mi, M. Kim, S. J. Cho, D. W. Park, H. Jiang, J. Lee, Y. Qiu, W. Zhou, Z. Cai, S. Gong & Z. Ma. Nat. Commun. 2015, 6, 7170.
10. L. Leonat, M. S. White, E. D. Głowacki, M. C. Scharber, T. Zillger, J. Rühling, A. Hübler, N. S. Sariciftci. J. Phys. Chem. C 2014, 118, 16813.
11. X. Du, Z. Zhang, W. Liu, Y. Deng. Nano Energy, 2017, 35, 299.

12. D. Zhao, Q. Zhang, W. Chen, X. Yi, S. Liu, Q. Wang, Y. Liu, J. Li, X. Li, H. Yu. ACS Appl. Mater. Interfaces, 2017, 9, 13213.
13. M. M. Hamedi, A. Hajian, A. B. Fall, K. Håkansson, M. Salajkova, F. Lundell, L. Wågberg, L. Berglund. ACS Nano, 2014, 8, 2467.
14. N. Mittal, R. Jansson, M. Widhe, T. Benselfelt, K. M. Håkansson, F. Lundell, M. Hedhammar, L. D. Söderberg. ACS Nano, 2017, 11, 5148.
15. S. Dai, Y. Chu, D. Liu, F. Cao, X. Wu, J. Zhou, B. Zhou, Y. Chen, J. Huang. Nat. Commun., 2018, 9, 2737.
16. M. Jämsä, S. Kosourov, V. Rissanen, M. Hakalahti, J. Pere, J. A. Ketoja, T. Tammelin, Y. Allahverdiyeva. J. Mater. Chem., 2018, 6, 5825.
17. M. Ioelovich. BioResources, 2008, 3, 1403.
18. A. Isogai. J Wood Sci, 2013, 59, 449.
19. T. Saito, Y. Nishiyama, J. L. Putaux, M. Vignon, A. Isogai. Biomacromolecules, 2006, 7, 1687.
20. N. Lin, A. Dufresne. Eur Polym J, 2014, 59, 302.
21. A. Isogai, T. Saito, H. Fukuzumi. Nanoscale, 2011, 3, 71.
22. H. Wang, Y. Wu, X. Yuan, G. Zeng, J. Zhou, X. Wang, J. W. Chew. Adv. Mater., 2017, 1704561, 1.
23. M. Ashton, K. Mathew, R. G. Hennig & S. B. Sinnott. J. Phys. Chem. C, 2016, 120, 3550.
24. M. Alhabeb, K. Maleski, B. Anasori, P. Lelyukh, L. Clark, S. Sin and Y. Gogotsi, Chem. Mater., 2017, 29, 7633–7644.
25. C. J. Brett, N. Mittal, W. Ohm, M. Gensch, L. P. Kreuser, V. Korstgens, M. Mansson, H. Frielinghaus, P. Muller-Buschbaum, L. D. Soderberg, S. V. Roth. Macromolecules, 2019, 52, 4721.
26. C. J. Zhang, S. Pinilla, N. McEvoy, C. P. Cullen, B. Anasori, E. Long, S.-H. Park, A. Seral-Ascaso, A. Shmeliov, D. Krishnan, C. Morant, X. Liu, G. S. Duesberg, Y. Gogotsi and V. Nicolosi, Chem. Mater., 2017, 29, 4848–4856.
27. S. Arabzadeh and A. Dolatabadi. J. Comput. Theor. Nanosci., 2008, 5, 2033.
28. A. Mandal, M. A. Jog, J. Xue and A. A. Ibrahim. Int. J. Heat Fluid Flow, 2008, 29 1494.
29. E. Kompinsky and E. Sher. J. Heat Transfer, 2015, 137, 051503.
30. F. Xiang, T. M. Givens and J. C. Grunlan. Ind. Eng. Chem. Res., 2015, 54, 5254.
31. W. Ohm, A. Rothkirch, P. Pandit, V. Korstgens, P. Muller-Buschbaum, R. Rojas, S. Yu, C. J. Brett, D. L. Soderberg, S. V. Roth. J. Coat. Technol. Res., 2008, 15, 4, 759.